Chemical Engineering Journal 537 (2026) 176362

Contents lists available at ScienceDirect

Chemical Engineering Journal

journal homepage: www.elsevier.com/locate/cej

CdS incorporation induced gate-opening in UiO-66-NH_2 for photocatalysis

Qi Li [a,1], Bryan Kit Yue Ng [b,c,1], Zhao-Xue Luan [d,1], Ping-Luen Baron Ho [b], Daniel Woodside [b], Xiyu Zhang [b], Christopher Foo [b], Pu Zhao [b], Tai-Sing Wu [e], Yun-Liang Soo [f], Mingjie Li [g], Xin-Ping Wu [d,*], Guangchao Li [a,h,i,**], Shik Chi Edman Tsang [a,b]

[a] Department of Applied Biology and Chemical Technology, The Hong Kong Polytechnic University, Hong Kong, 999077, China
[b] Department of Chemistry, University of Oxford,Oxford, OX1 3QR, United Kingdom
[c] Repolywise Limited, Centre of Innovation and Enterprise, Oxford University Begbroke Science Park, Kidlington, OX51PF, United Kingdom
[d] State Key Laboratory of Green Chemical Engineering and Industrial Catalysis, Centre for Computational Chemistry and Research Institute of Industrial Catalysis, School of Chemistry and Molecular Engineering, East China University of Science and Technology, Shanghai, 200237, China
[e] National Synchrotron Radiation Research Center, 101 Hsin-Ann Road, Hsinchu, 30076, Taiwan
[f] Department of Physics, National Tsing Hua University, Hsinchu, 30013, Taiwan
[g] Department of Applied Physics, The Hong Kong Polytechnic University, Hong Kong, 999077, China
[h] The Hong Kong Polytechnic University, Shenzhen Research Institute, Shenzhen, 518057, China
[i] PolyU-Daya Bay Technology and Innovation Research Institute, The Hong Kong Polytechnic University, Huizhou, 516000, China

ARTICLE INFO

Keywords:
Gate-opening effect
Liner rotation
UiO-66-NH_2 MOF
CdS
Composite

ABSTRACT

Integrating semiconductors into metal-organic frameworks (MOFs) typically compromises porosity due to pore blockage or coverage. Conversely, we report a CdS/UiO-66-NH_2 composite, achieving a 1.5-fold increase in specific surface area. Through in-situ synthesis, CdS clusters are embedded into the tetrahedral pores of UiO-66-NH_2. Structural analysis utilizing Rietveld-refined synchrotron X-ray diffraction (SXRD) and density functional theory (DFT) reveals the confined CdS clusters modulate the rotation of organic linkers, synchronously expanding the framework by a guest-induced gate-opening effect. In addition, CdS/UiO-66-NH_2 heterostructure significantly facilitates efficient charge carrier separation. Consequently, the optimized CdS/UiO-66-NH_2 exhibits a more than doubled photocatalytic water splitting rate compared to pristine UiO-66-NH_2. This work offers molecular-level insights into leveraging structural flexibility for constructing high-efficiency photocatalysts.

1. Introduction

With the escalating global energy demand and the imperative to mitigate climate change, hydrogen production via solar-driven photocatalytic water splitting has emerged as a promising strategy for sustainable energy generation. [1–3] Among the various photocatalysts developed, metal–organic frameworks (MOFs) have attracted significant attention due to their highly ordered structures, tunable pore sizes, and exceptionally high specific surface areas (SSA). [4–8] Specifically, the zirconium-based UiO-66 family stands out for its exceptional chemical and thermal stability in aqueous environments. While the pristine UiO-66 absorbs primarily in the UV region, its derivative, UiO-66-NH_2, incorporates amino groups that function as light-harvesting antennas, effectively narrowing the bandgap for visible-light response. [9–11] However, despite these advantages, UiO-66-NH_2 alone still suffers from rapid photogenerated electron-hole recombination and slow charge transfer kinetics, which severely restricts its photocatalytic efficiency. [12–14]

To overcome these intrinsic limitations, the construction of heterojunctions by integrating MOFs with narrow-bandgap semiconductors, such as Cadmium Sulfide (CdS), has become a promising strategy. [15–18] The formation of a semiconductor/MOF heterojunction can facilitate spatial separation of charge carriers and extend the light absorption range. Nevertheless, a critical limitation still exists in this field: the conventional semiconductor/MOF composites suffer from blockage or coverage of MOF pores by the cocatalyst particles, reduced effective pore diameter, and the burial of active catalytic sites. Consequently, the development of new porous semiconductor/MOF composites that can

* Corresponding author.
** Correspondence to: G. Li, Department of Applied Biology and Chemical Technology, The Hong Kong Polytechnic University, Hong Kong, 999077, China.
E-mail addresses: xpwu@ecust.edu.cn (X.-P. Wu), guangchao.li@polyu.edu.hk (G. Li).
[1] These authors contributed equally

https://doi.org/10.1016/j.cej.2026.176362
Received 7 January 2026; Received in revised form 16 March 2026; Accepted 16 April 2026
Available online 17 April 2026

effectively promote the separation of photogenerated carriers without significant pore blockage and reduction in accessible surface area is highly desirable and technologically important.

Recent studies suggest that the structural flexibility of MOFs, such as linker rotation or framework breathing, could offer a pathway to modulate porosity dynamically. [19–21]. For instance, the MIL-53 family exhibits remarkable breathing flexibility, where the framework can reversibly expand or contract in response to guest molecule adsorption or desorption. [26] In addition, Jimenez et al. reported the rotation of imidazole linkers in ZIF-8 structure induced enlargement of pore windows, under conditions of gas adsorption or high pressure (i.e., 14,700 bar), thereby allowing the adsorption of larger molecules than anticipated. [27] Modrow et al. synthesized a pillared-layer MOF ($[Zn_2(2,6\text{-ndc})_2(azo\text{-bipy})]_n$) with light-controlled structural flexibility. Upon exposure to light with a wavelength of 365 nm, this material undergoes a structural transformation wherein the linker isomerizes from the thermodynamically stable *trans* form to the *cis* form. [28] While external stimuli (e.g., gas adsorption, light, temperature and pressure) are known to induce gate-opening effects that expand pore windows, leveraging this flexibility to accommodate co-catalysts without sacrificing surface area has rarely been explored in photocatalytic system design. [22–25] Although structural alterations and unusual increases in specific surface have been observed on semiconductor/MOF composites, [29,30] in-depth study on sorption mechanisms and structural responses of MOFs at the molecular level are lacking.

In this study, we address the aforementioned limitations by constructing a CdS/UiO-66-NH_2 photocatalyst with through a bottom-up co-catalyst synthesis strategy. Unlike conventional composites that suffer from surface area reduction, our approach utilizes the affinity between Cd^{2+} precursors and the amino groups ($-NH_2$) of the MOF linkers to anchor CdS clusters within the framework pores. We demonstrate that this internal growth of CdS clusters induces a gate-opening effect by modulating linker rotation, leading to an unexpected increase in SSA and pore volume compared to the pristine UiO-66-NH_2. Structural characterization via X-ray diffraction, absorption techniques, along with microscopy images reveals the diffusion of Cd^{2+} into MOF pores with subsequent CdS nucleation. Synchrotron X-ray powder diffractions (SXRD) and density functional theory (DFT) studies elucidate that the embedded CdS clusters modulate the rotational flexibility of organic linkers in UiO-66-NH_2. This ligand mobility enables gate-opening behavior and synchronous SSA increase as confirmed by Brunauer-Emmett-Teller (BET) analysis. Furthermore, photoelectronic characterizations show the enhanced visible-light absorption and efficient charge carrier separation. The optimized CdS-decorated UiO-66-NH_2 catalyst exhibits over a 200% enhancement in photocatalytic water splitting performance versus pristine MOF, which is attributable to the increased specific surface area with exposed active sites as well as synergistically improved light absorption and charge carrier dynamics.

2. Experimental section

2.1. Chemicals

All chemicals and solvents in this work were commercially available with 98% purity or above, and used as received. The chemicals used in sample synthesis were obtained from Sigma Aldridge and Alfa Aesar, including Zirconium (IV) chloride (≥99.5%), 2-aminoterephthalic acid (99%), glacial ethanoic acid (99.8%) and dimethylformamide (≥99.9%), cadmium nitrate tetrahydrate (≥99%), thioacetamide (98%) and triethanolamine (98%).

2.2. Synthesis of UiO-66-NH_2

545 mg of 2-aminoterephthalic acid, 668 mg of $ZrCl_4$ and 14 mL of ethanoic acid was added into 200 mL of Dimethylformamide (DMF) in a 250 mL borosilicate glass reagent bottle. The resultant mixture was sonicated for 10 min, and then heated to 120 °C in an oven for 24 h. Once removed from the oven and allowed to cool, the project was washed three times with DMF, followed by three times with ethanol, before being dried at 60 °C in a vacuum oven overnight.

2.3. Synthesis of CdS/UiO-66-NH_2

480 mg of UiO-66-NH_2 was suspended in 25 mL of deionized (DI) water with vigorous stirring for 30 min. 1.744 g of $Cd(NO_3)_2{\cdot}4H_2O$ was dissolved separately in 15 mL of DI water and then added dropwise to the UiO-66-NH_2 suspension. Finally, a varying amount of thioacetamide (TAA) was added to 10 mL of DI water and added dropwise to the suspension. The amount of TAA added are: 0 mg for 0.1Cd, 21.2 mg for 0.2Cd, 84.9 mg for 0.8Cd, 169.9 mg for 1.8Cd and 339.7 mg for 2.3Cd. The resultant mixture was heated in an oil bath to 60 °C and stirred for 3 h, before being washed with methanol x 3 and DI x 3. The solid samples will then be centrifuged and collected, dried in vacuum over at 60 °C.

CdS was synthesized according to the method used to synthesise the 2.3Cd catalyst; however, no UiO-66-NH_2 was added during the procedure.

2.4. Evaluation of photocatalytic performance

The photocatalytic activity was mainly determined by the hydrogen evolution rate (μmol h^{-1} g^{-1}) from water splitting. Reactions were carried out in a closed 25 mL stainless steel autoclave system (Parr, United States) equipped with two quartz windows (with a diameter of 10 mm and a thickness of 18 mm). Control experiments reveal that no hydrogen was produced without catalyst and light irradiation under detection limit. In a typical activity test, 25 mg of catalyst was added to 7.2 mL DI water and 0.8 mL of TEOA in a quartz lining (20 mm i.d. × 24 mm o.d. × 52 mm height), then the autoclave was purged with 6 bar of Ar gas after being tightly sealed for 8 times. The mixture in the reactor would then be allowed to heat up to 120 °C under vigorous magnetic stirring (750 rpm). Xenon lamp (300 W, Industrial Grade Arc Lamp with Dual Plano-Convex Lens, Fused Silica, Ozone-free, Newport) was then used to shine through the quartz windows at 10 cm. After 1.5 h reaction, the autoclave was cooled down naturally to room temperature. The content of hydrogen was measured by gas chromatography (GC) equipped with thermal conductivity detectors (TCD) with He as the carrier gas, respectively.

To evaluate the stability and reusability of the catalyst, cyclic photocatalytic hydrogen evolution experiments were conducted under identical conditions to the standard activity test described above. After the completion of the first run, the used catalyst was recovered by centrifugation and washed four times with deionized water to remove residual sacrificial agents. The collected solid was then re-dispersed in a fresh TEOA aqueous solution (7.2 mL water +0.8 mL TEOA), followed by thorough Ar purging. This process was repeated for five consecutive runs under identical reaction conditions.

2.5. Density functional theory (DFT) calculations

Density functional theory (DFT) calculations were performed using the PBE0 functional. [31] The wavefunctions were represented using the DZVP MOLOPT basis set [32] and the Goedecker-Teter-Hutter (GTH) pseudopotentials. [33] An energy cutoff of 600 Ry and Γ point sampling of the Brillouin zone were used. The convergence criterion for electron minimization was set to 10^{-4} eV, and the force convergence criterion was set to 0.02 eV/Å. Excited-state calculations were performed using the time-varying density functional perturbation theory (TDDFPT). [34] All calculations were performed in the CP2K package. [35]

The structure of UiO-66-NH_2 was constructed by functionalizing the linkers in the primitive cell of UiO-66 using the NH_2 group. The structure of CdS/UiO-66-NH_2 was constructed by incorporating a CdS cluster into the tetrahedral pore of UiO-66-NH_2. Five representative CdS clusters,

including Cd_3S_3, $(Cd_3S_3)_2$, $(Cd_3S_3)_3$, Cd_4S_4 (C_{2V}), and Cd_4S_4 (T_D) reported in ref. [36] (Fig. S24), were considered. The relative stabilities of the CdS clusters were quantified by calculating the average energies (E_{avg}) of the CdS units within those clusters:

$$E_{avg} = \frac{E_{tot}}{n}$$

where E_{tot} is the calculated total energy of a CdS cluster, and n is the number of CdS units within the cluster. Considering the relative stabilities of the CdS clusters and the size of the tetrahedral pore of UiO-66-NH_2 (~7 Å), Cd_4S_4 (T_D) was selected for further investigations.

Binding energy E_B was calculated according to the following expression:

$$E_B = E[CdS/UiO-66-NH_2] - E[CdS] - E[UiO-66-NH_2]$$

where $E[CdS/UiO-66-NH_2]$ is the DFT-calculated total energy of CdS/UiO-66- NH_2, $E[CdS]$ is the total energy of the isolated CdS cluster, and $E[UiO-66-NH_2]$ is the total energy of the relaxed pristine UiO-66-NH_2 framework.

3. Results and discussion

3.1. Structural characterization

A series of one-pot syntheses of CdS/UiO-66-NH_2 were carried out using a constant amount Cd source (Cadmium nitrate, $Cd(NO_3)_2$) and varying amounts of S source (TAA), starting from zero and gradually increasing. In this synthesis method, the aggregation of CdS is a consequence of the reaction between Cd and thiol upon hydrolysis of TAA. [37,38] Inductively-coupled plasma-mass spectrometry (ICP-MS) was performed on a series of samples to quantify the loading amounts of Cd and S onto UiO-66-NH_2, and presented the results in weight percentage (Table S1). As the amount of TAA added increased, the loading amount of Cd showed an upward trend. This observation highlights the strong affinity of Cd for S, as predicted by the hard soft acid-base theory, [39] and is evidenced by the enhanced Cd incorporation into the MOF in the presence of TAA. The samples are then named according to the weight percentage of Cd present in each sample (0.1Cd, 0.2Cd, 0.8Cd, 1.8Cd, and 2.3Cd/UiO-66-NH_2). For clarity, the UiO-66-NH_2 suffix in the sample names is omitted in subsequent paragraphs.

Structural characterizations are firstly performed to elucidate the Cd species present in the catalysts and their interactions with the MOF support. Firstly, the structural integrity and the identity of Cd species deposited on MOF were studied with X-ray diffraction (XRD, Fig. 1a). The diffraction patterns of the synthesized catalysts are consistent with the literature, [40] and the sharp and narrow peaks indicate again that the high crystallinity has been maintained upon Cd and S decoration. The porosity and SSA upon introduction of Cd and S species were investigated through BET analysis. The nitrogen adsorption-desorption isotherms of the synthesized samples all show characteristics of type II isotherms (Fig. S1), indicating the presence of a large number of micropores. [41] The BET SSA of pristine UiO-66-NH_2 is 818.8(27) $m^2\ g^{-1}$, which agrees with values in reported in the literature. [42,43] All Cd decorated UiO-66-NH_2 samples are found to bear higher surface area compared to the pristine counterpart (Fig. 1b). Among them, 1.8Cd and 2.3Cd samples with high Cd species loading are found to possess significantly higher SSAs of 1176.3(47) and 1025.0(41) $m^2\ g^{-1}$, respectively. The DFT pore size distributions (>10 Å) generated based on the adsorption isotherms of all samples are shown in Fig. 1c. The primary and pronounced peaks for mesoporous UiO-66-NH_2 are observed at 12 Å, 15.5 Å and 19 Å, which are presumed to be attributed to the octahedral pores and defect-related nanoregions, respectively. [44,45] Upon the loading of Cd species, the pore distribution of the UiO-66-NH_2 remains unchanged, but the pore volume of the composite materials significantly increases (Fig. S2). For the octahedral mesopores with a width of 12 Å, the pore volume initially increases and subsequently decreases with increasing Cd loading, which is speculated to be associated with the interaction between the Cd species and the organic linkers. In addition, CO_2 adsorption–desorption measurements were conducted over pristine UiO-66-NH_2 and optimal 1.8Cd to further probe the microporosity (< 1 nm) that may not be fully accessible to N_2 at 77 K due to diffusion/kinetic limitations. As presented in Table S2 and the

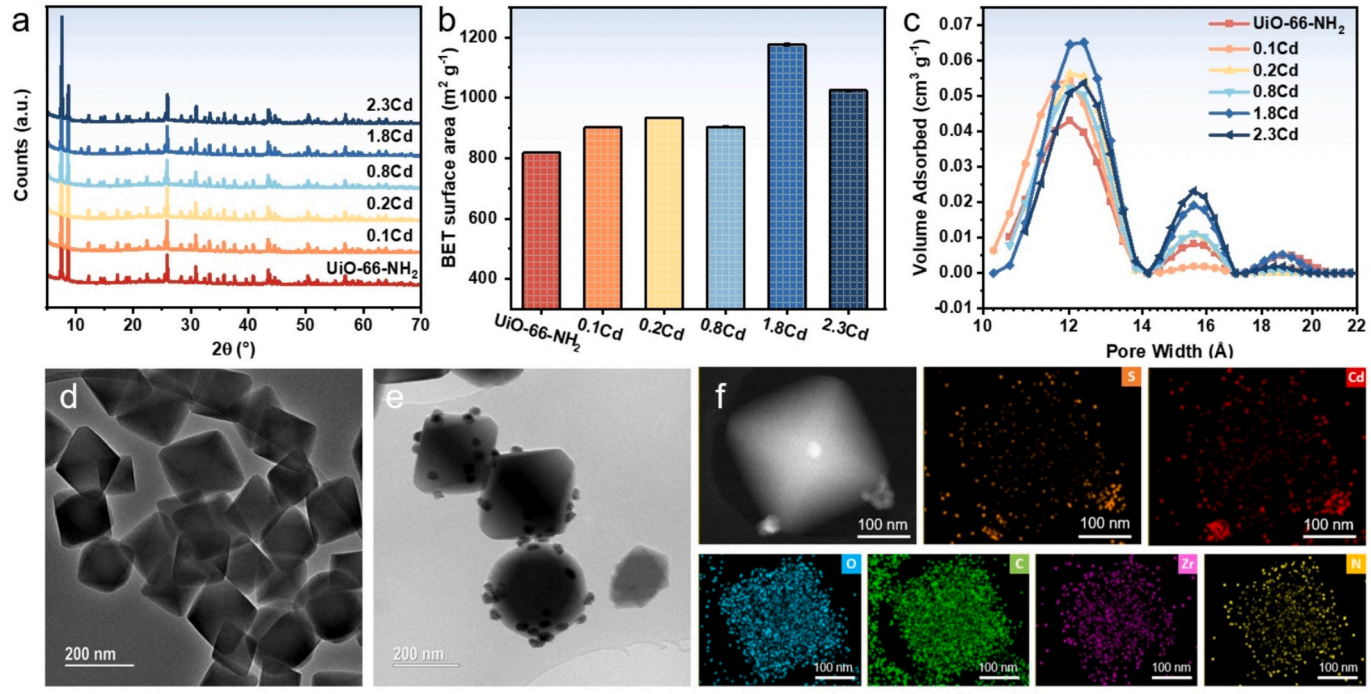

Fig. 1. (a) XRD pattern, (b) BET surface area, and (c) Pore size distribution of the different samples. TEM images of (d) UiO-66-NH_2 and (e) 1.8Cd. (f) HAADF-STEM image for 1.8Cd with its EDX mapping for S, Cd, O, C, Zr, and N elements.

corresponding pore analysis plots in Fig. S3, the CO_2-derived micropore parameters showed a clear change in micropore accessibility upon Cd decoration. Specifically, the H—K median pore width slightly increases from 0.6732 nm for UiO-66-NH_2 to 0.6892 nm for 1.8Cd, suggesting a widening of the micropore. The Dubinin–Astakhov (D-A) limiting micropore volume increases markedly from 0.3098 to 0.4407 $cm^3\ g^{-1}$, accompanied by a substantial rise in D-A micropore surface area from 751.2 to 992.6 $m^2\ g^{-1}$. These results indicate that the introduced Cd species can enhance the accessibility/availability of micropores.

The morphologies of UiO-66-NH_2 before and after Cd decoration were investigated by Scanning electron microscopy (SEM) and transmission electron microscopy (TEM). The cubic morphology of UiO-66-NH_2 is confirmed by TEM (Fig. 1d) and SEM (Fig. S4), indicated by the truncated octahedra showing (100) and (111) crystallographic facets. Such morphologies are retained in 0.1Cd, 0.2Cd, 0.8Cd, 1.8Cd, and 2.3Cd as shown by their TEM images (Fig. S5–9). Distinct dark spots are observed on the surface of 1.8Cd (Fig. 1e and Fig. S8) and 2.3Cd (Fig. S9) samples. Upon closer examination of these spots, a fringe spacing of 3.3 Å was identified, which corresponds to the (111) plane of cubic CdS (Fig. S9). [46] The fact that such CdS nanoparticles generate no new XRD peaks, indicates that the CdS nanoparticles possess short-range crystallinity but lack the long-range order detectable by XRD due to their small crystallite size and high dispersion. Such surface-decorated CdS particles are frequently observed in the 1.8Cd and 2.3Cd samples, whose statistical analysis reveals average particle diameters of 30.9 ± 6.1 and 57.4 ± 14.1 nm, respectively (Fig. S11). Energy dispersive X-ray (EDX) elemental mapping of C, N, O, S, Cd and Zr for 0.1Cd, 0.2Cd, 0.8Cd, 1.8Cd and 2.3Cd samples are presented in Fig. 1f and Fig. S12–15. For improved clarity, the EDX mapping was subjected to a 40% increase in brightness. For the 0.1Cd that only contained the Cd source during the preparation process, it can be observed that the C, N, O, Zr and Cd elements are uniformly distributed throughout the material (Fig. S12). The Cd element, due to its lower content, has a relatively weaker signal. For the 0.2Cd and 0.8Cd samples with low S source addition, all elements including S are observed to be well distributed. In the case of 1.8Cd and 2.3Cd, similar elemental distributions within the MOF framework are observed, while S and Cd elements are found to aggregate on the surface, corresponding to the presence of CdS nanoparticles on the surface of UiO-66-NH_2 framework.

To further investigate the coordination environment of Cd species in the samples, Cd K-edge X-ray absorption spectroscopy (XAS) were performed. According to our synthesis method, the isolated Cd^{2+} ions would have been washed away during the synthesis process, the possible elements coordinating to Cd include O from aqua or hydroxide, N from amino group of the from the 2-aminoterephthalic acid organic linkers, or S from TAA. The similar X-ray scattering factors of N and O make it difficult to distinguish between these two elements. Therefore, the subsequent discussion will focus on O/N together and S as the possible first shell neighbours of Cd. As shown in Fig. 2a, the intensity of the white line near the absorption edge decreases with increasing Cd loadings, indicating an elevated electron density of Cd in the catalysts. This observation is attributed to a coordination change from predominantly Cd–O/N to Cd—S. The R-space EXAFS data are shown in Fig. 2b and Fig. S16, with the k-space data and their fitting parameters available in Fig. S17 and Table S3. Data fitting performed on the EXAFS data reveals a gradual shift from Cd–O/N to Cd—S bonds quantitatively as the loading of Cd increases. For optimal reliability, k^1, k^2, and k^3-weighted spectra are simultaneously fitted in R-space, with more details on the fitting method available in the Supplementary Information. For the 0.1Cd sample, Cd–O/N coordination environment with a coordination number of 5.44(77) at a bond length of 2.27(1) Å was observed. It is worth noting that no Cd—Cd scattering is observed, this further suggests that Cd is incorporated in UiO-66-NH_2 MOF as a single site. With no sulphur source added during synthesis of 0.1Cd, the existence of single-site Cd suggests that Cd^{2+} ions are capable of entering the pores and anchoring onto UiO-66-NH_2. These single-site Cd^{2+} are likely coordinated to amine or hydroxyl group from MOF, H_2O or OH^- ions for charge balancing. The 0.2Cd sample sees a reduction in Cd–O/N coordination to 1.96(45) at 2.22(3) Å, along with the emergence of Cd—S scattering to a coordination number of 1.51(69) at 2.54(3) Å. This shift in bonding environment marks the formation of CdS alongside the single site previously mentioned, as TAA is added in the synthetic process of 0.2Cd. For samples with a higher sulphur source added, the size and amount of CdS increase compared to 0.2Cd as indicated by increased Cd—S scattering, with 4.00(39) at 2.51(1) Å, 4.05(39) at 2.52(1) Å and 3.93(35) at 2.52(1) Å for 0.8Cd, 1.8Cd and 2.3Cd, respectively. This

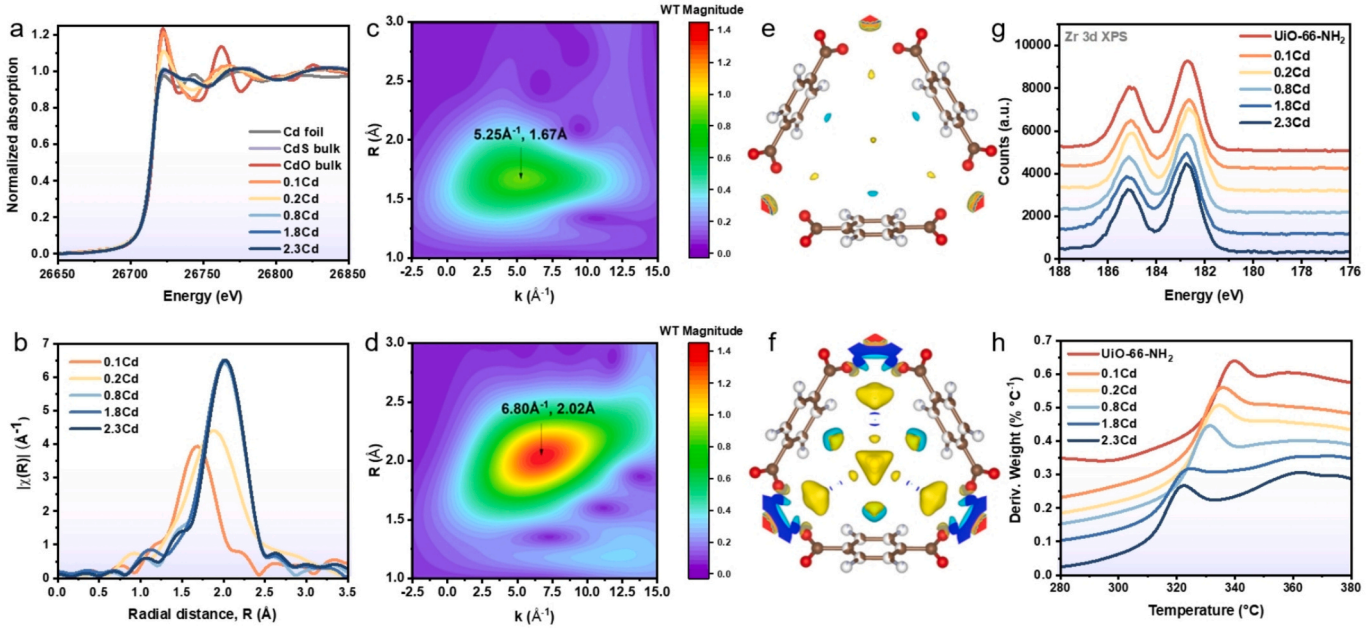

Fig. 2. (a) X-ray absorption near-edge region, and (b) k^3-weighted R-space EXAFS data of obtained samples. Wavelet transform of EXAFS data for (c) 0.1Cd and (d) 1.8Cd. The electron density difference generated from SXRD data for (e) UiO-66-NH_2 and (f) 1.8Cd. Colour code: Brown = C, Red = O, White = H, Yellow = electron density, Blue = electron hole. Isosurface = 0.3. (g) Zr 3d XPS spectra, and (h) Weight derivative at 280–380 °C obtained from TGA for the series of samples.

shows clear evidence of increased CdS particle size and quantity. Meanwhile, as the CdS aggregate, the change from octahedral to tetrahedral coordination favored by d-p mixing can be recognized. [47] This observation aligns with CdS nanoparticles formation in the material as cubic CdS exhibits the wurtzite structure, with Cd—S bond lengths of around 2.5 Å. Wavelet transform (WT) of the Extended X-ray absorption fine structures (EXAFS) data showed a gradual shift of peak position from 5.25 $Å^{-1}$, 1.67 Å for 0.1Cd (Fig. 1c), to 6.60 $Å^{-1}$, 2.02 Å for 1.8Cd (Fig. 1d). The progressive change from Cd–O/N to Cd—S coordination is manifested by the increase in both k (atomic number) and R (radial distances) of the first shell neighbours with respect to Cd. WT for 0.2Cd, 0.8Cd and 2.3Cd is available in the Fig. S18.

For the 1.8Cd and 2.3Cd samples with high TAA addition in the synthesis process, in addition to the distinct CdS nanoparticles formed on the surface, the porosity of UiO-66-NH_2 enables the modification of the intrinsic adsorption sites within the framework, which promote the diffusion of Cd and S source and the formation of CdS species in pores. To further clarify the presence and location of the CdS species inside the pores, synchrotron XRD (SXRD) was performed on UiO-66-NH_2 along with the 1.8Cd and 2.3Cd samples. The results suggest that the lattice parameter decreases from 20.832011(55)Å to 20.811634(61)Å and 20.805626(64)Å for UiO-66-NH_2,1.8Cd and 2.3Cd, respectively, with increasing Cd loading (Table S5). This trend may be attributed to the influence of Cd species in enhancing the electrostatic interactions within the framework. [3] The electron density difference generated from SXRD data for UiO-66-NH_2, 1.8Cd and 2.3Cd is displayed in Fig. 2e-f and Fig. S19. Additional electron density within the pores is observed on 1.8Cd and 2.3Cd. For clarity, the isosurface of electron density in the tetrahedral pores is depicted, and the electron difference map without the framework is made available in Fig. S20. This extra electron density is attributed to CdS species in the pores and is found in close proximity to the organic linkers, suggesting a potential chemical interaction between the organic linkers and the CdS species confined within the pores.

The oxidation states of Zr present in the series of samples are analysed by X-ray photoelectron spectroscopy (XPS, Fig. 2g and Table S5). The spin-orbit coupling $3d_{3/2}$ and $3d_{5/2}$ peaks for Zr in all samples emerge at 185.1 and 182.7 eV respectively, which correlates well with the literature. [48] This suggests the $Zr_6O_4(OH)_4$ pillars of UiO-66-NH_2 remain untouched and the CdS species do not coordinate to the hydroxyl group in place of the inherent missing linker defects, [49] as the introduction of metal species on Zr-oxo clusters has been shown to shift the binding energy for Zr probed by XPS. [50] The Cd species present in the pores can therefore be concluded to be chemically unrelated to the Zr-oxo cluster. These Cd species are likely coordinated to amine groups present in the MOF structure.

Furthermore, the Cd species within the pores and their impact on the stability of UiO-66-NH_2 were further investigated through thermogravimetric analysis (TGA) (Fig. S22). The derivative of the weight is used to further zooming in to the 280–380 °C (Fig. 2h). The temperature corresponding to the structure collapse of MOF, determined as the temperature with highest rate of mass loss, decreases with increasing Cd present from 339.7 °C in UiO-66-NH_2 to 322.6 °C in 2.3Cd. Single-site Cd^{2+} (in the case of low loading) or CdS (high loading) coordinated to the amino group of the organic linker draws electron density away from it, hence weakening the electrostatic interaction between the anionic linker and cationic Zr^{4+}-based metal-oxo clusters.

The above structure characterization revealed the presence of Cd species within the pores and on the surface of UiO-66-NH_2. The Cd species in pores can be rationalized by the fact that Cd^{2+} ion with an ionic radius of 0.97 Å can easily diffuse into its pores and coordinate to the amino group on the organic linker as well as the S^{2-} ions generated from the hydrolysis of TAA. As for the CdS nanoparticles present on the surface, with more TAA added in the synthesis process, the generated CdS will aggregate before coming into contact with MOF, resulting in CdS grafted on the surface. [51] For either single-site Cd^{2+} or CdS particles, the Lewis basic amino group on the organic linker of UiO-66-NH_2 has provided anchoring sites.

3.2. Structure-SSA relationship

Having clarified the different Cd species incorporated in the MOFs, subsequent investigations were conducted to elucidate the underlying mechanisms responsible for the enhanced SSA of composites. It is widely acknowledged that any modification may alter the connectivity between metal nodes and organic linkers, potentially blocking the pores present in MOFs. However, it has been reported in the literature that the surface area of UiO-66 series MOFs can increase upon post-synthetic modification. [29,30] Additionally, it has been demonstrated that the heteronuclear species can induce a gate-opening effect of MOF materials, thereby modifying their crystal structure. [52–54]

To gain detailed insight into the structural modification induced by CdS decorations on UiO-66-NH_2, SXRD data for both the pristine UiO-66-NH_2 and the CdS decorated 1.8Cd samples were analysed by Rietveld refinement. Based on the above characterization results, the $Zr_6O_4(OH)_4$ clusters have been held untouched, with the only degrees of freedom allowed for the rotation of the organic linker. The observed, calculated, and difference in SXRD intensity, and the structure of UiO-66-NH_2 and 1.8Cd are presented in Fig. 3a and c. The crystallographic data and details of are shown in Table S6. For pristine UiO-66-NH_2, a dihedral angle of 0° can be observed (Fig. 3b and Fig. S22a). A similar Rietveld refinement analysis is performed on the SXRD data of 1.8Cd (Fig. 3c). The careful refined structure of the 1.8Cd sample, which has refinement parameters within acceptable experimental errors, is shown in Fig. 3d and Fig. S23b. It was observed that the dihedral angles of the organic linkers present in the MOF vary according to the loading of CdS in the sample. Comparing with pristine UiO-66-NH_2, in 1.8Cd sample, CdS nanocluster was observed in the tetrahedral pore of framework. Cd sites with atom site occupancy (SOP) of 0.05 (Cd1) and 0.03 (Cd2) were observed (Table S8). Furthermore, a rotation of the organic linker by 25.8° can be observed on 1.8Cd (Fig. 3 and Fig. S23). The Rietveld refinements of the SXRD data reveals increased dihedral angles of the organic linkers present in UiO-66-NH_2 MOFs, which underpins the increased surface area for 1.8Cd.

To further verify the underlying cause of the observed differences in dihedral angles (Fig. 3e) in the optimized Rietveld-refined models, DFT calculations were conducted. The CdS species diffused through the tetrahedral pore of UiO-66-NH_2 was modelled by a Cd_4S_4 cluster (i.e., Cd_4S_4 (T_D) in Fig. S24), with consideration given to the relative stabilities of five representative CdS clusters (Fig. S24 and Table S9) and the size of the tetrahedral pore of UiO-66-NH_2 (~7 Å). [55] Table 1 lists a comparison of the dihedral angles ϕ for the linkers in UiO-66-NH_2 and CdS/UiO-66-NH_2 (Fig. 3f and g).The dihedral angles for the six linkers that comprise the tetrahedral pore of UiO-66-NH_2 typically fall below 10°; the averaged dihedral angle is calculated to be 7.62°. The incorporation of CdS into the tetrahedral pore of UiO-66-NH_2 results in electron transfer of 3.98 |e| (Hirshfeld charge) from the MOF to CdS and the formation of four Cd—N bonds (Fig. 3g and Table 2), which subsequently rotates the corresponding linkers and increases the corresponding dihedral angles, leading to an elevated averaged dihedral angle of 18.47° (Table 1). Notably, the binding energy of CdS/UiO-66-NH_2 is −1.31 eV, indicating energetically favorable confinement of CdS in the tetrahedral pore and providing a driving force for the CdS-induced gate-opening effect. This results in a more open gate of CdS/UiO-66-NH_2 in comparison to UiO-66-NH_2, which is consistent with the experimental findings. Additionally, the impact of photoexcitation on the configuration of CdS/UiO-66-NH_2 was examined. Table S10 lists the dihedral angles for the six linkers in CdS/UiO-66-NH_2 in both ground state and excited state. Despite the occurrence of MOF-to-CdS charge transfer in the first excitation, the dihedral angles demonstrate insignificant changes after excitation, showing excellent stability under light conditions.

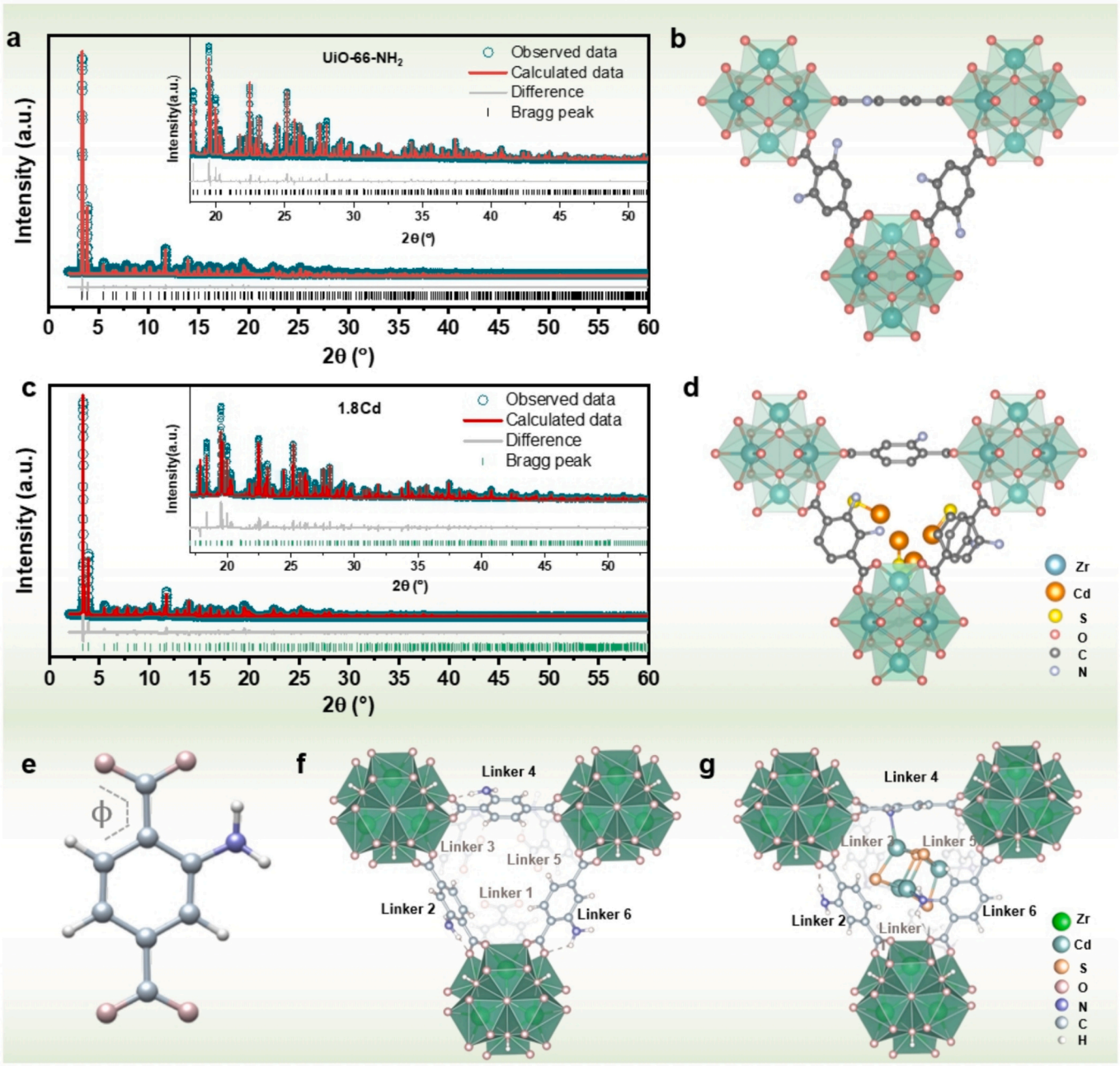

Fig. 3. Observed, calculated and difference in SXRD intensity for Rietveld Refinement of (a) pristine UiO-66-NH_2 and (c) 1.8Cd. The Rietveld refined structural model showing the rotation viewed in the plane of the carboxylate of the organic linker on top for (b) UiO-66-NH_2, and (d) 1.8Cd. Hydrogen and adsorbed water O atoms have been omitted for clarity. (e) The structure of the linker with the dihedral angle ϕ under investigation. The calculated most stable configurations of (f) UiO-66-NH_2 and (g) CdS/UiO-66-NH_2. The six linkers studied are labelled in (f) and (g).

3.3. Optical characteristics

Having clarified the different Cd species incorporated in the MOFs and the increase in SSA caused by the gate-opening effect, optical characterisations were then implemented to inspect the light response of CdS/UiO-66-NH_2 composites. UV–Vis spectroscopy was conducted on all samples (Fig. 4a). The absorption band around 265 nm observed in UiO-66-NH_2 can be ascribed to the overlap of the π–π* transition of the organic linker and the absorption of the Zr oxo cluster. The absorption in the 300-400 nm region is attributed to the organic linker-based n to π* transition. [56,57] Incorporate with only Cd^{2+} ions in the 0.1Cd sample results in increased UV absorbance whilst absorbance in the visible regions decreased slightly. As CdS loading into UiO-66-NH_2 is increased, a new absorption edge (450–550 nm) emerges, and pushes further into the visible range, which can be attributed to the absorption of CdS. The gradual improvement of light absorption has been recognized as the loading of Cd increases, signifying the improvement in adsorption of light from both single-site Cd^{2+} or CdS species. The observed red shift in absorption indicates the CdS/UiO-66-NH_2 catalysts can absorb more visible light, resulting in a greater number of photoinduced excitons than in UiO-66-NH_2, which will make photocatalysis more efficient. In addition, the emergence of the second absorption edge further confirms the existence of the two phases within the composite. The Tauc plots were generated to probe the band structure of obtained catalyst (Fig. S25). The Cd-decorated MOFs have similar band gap energies to the parent UiO-66-NH_2 at ~2.94 eV, indicating the band gap is virtually

Table 1
Dihedral angles (ϕ, °) for the six linkers that comprise the tetrahedral pores of UiO-66-NH_2 and CdS/UiO-66-NH_2 and the averaged dihedral angles (ϕ_{avg}, °).

	ϕ for different linker						ϕ_{avg}
	Linker 1	Linker 2	Linker 3	Linker 4	Linker 5	Linker 6	
UiO-66-NH_2	10.69	4.21	11.71	3.53	8.42	7.18	7.62
CdS/UiO-66-NH_2	1.99	2.02	26.40	26.83	27.17	26.72	18.47

Table 2
Bond lengths (d, Å) of the four newly formed Cd—N bonds after the incorporation of the Cd_4S_4 (T_D) cluster into the tetrahedral pore of UiO-66-NH_2.

N in linker #	3	4	5	6
d	2.49	2.55	2.42	2.42

unaffected by the introduction of Cd species into the framework. The band gaps for CdS in CdS/UiO-66-NH_2 could be calculated for the 1.8Cd and 2.3Cd samples, with values of 2.34 eV. The Mott-Schottky plots of as-obtained CdS and UiO-66-NH_2 were displayed in Fig. S26, the positive slop indicated their n-type nature. The calculated flat band potentials of CdS and UiO-66-NH_2 were − 0.92 and − 0.39 V versus NHE, respectively. Based on the above characterization and results, the energy band structures of CdS/UiO-66-NH_2 were depicted (Table S11).

To examine the behaviors of charge separation in obtained photocatalysts, steady-state photoluminescence (PL) measurements were conducted under 375 nm excitation. As the Cd loading into UiO-66-NH_2 increases, a significant decrease in the PL intensity is observed (Fig. 4b), suggesting the incorporated Cd species gradually inhibited the recombination of photogenerated carriers, thereby reducing the fluorescence intensity. This is further evidenced by a Stern-Volmer plot of I_0/I against combined wt% of Cd from ICP, which gives a linear trend with a high R-factor of 0.998 (Fig. S27). [58,59] To further validate the influence of different Cd species and confirm the behavior of charge carrier transfer, the PL spectra of 0.1Cd, 0.2Cd, 0.8Cd, 1.8Cd, 2.3Cd, and UiO-66-NH_2 were normalized and deconvoluted to facilitate comparison. The normalized PL spectra of 0.1Cd and 0.2Cd overlap with that for UiO-66-NH_2 with no observable change (Fig. S28 a). Adversely, for 0.8Cd, 1.8Cd, and 2.3Cd, where CdS clusters are present within the pores or CdS nanoparticles are formed on the surface, the peak of fluorescence gradually shifts to the right from 455 to 466 nm, along with the formation of a shoulder at around 500 nm. [62] To quantify the peak shoulder, two Gaussian peaks at 455 nm and 492 nm are used to fit the normalized PL data for 0.8Cd, 1.8Cd and 2.3Cd (Fig. S28 b), with the corresponding fitting parameters provided in Table S12. The peak at 455 nm originates from the n to π^* transition in UiO-66-NH_2, whereas the 492 nm peak is ascribed to charge carrier recombination on CdS species. [9,63] The normalized deconvoluted spectra show a clear reduction of the 455 nm peak with increased CdS loading whilst the 492 nm peak increases in intensity. This further confirms the decreasing PL of UiO-66-NH_2 with the increase of CdS due to heterojunction formation and improved charge separation. In addition, electrochemical impedance spectra (EIS) measurement is performed to further confirm the charge separation. As depicted in Fig. 4c, owing to improved electron conductivity, the arc radii of 0.8Cd, 1.8Cd and 2.3Cd samples are much smaller than those of UiO-66-NH_2, 0.1Cd and 0.2Cd, indicating a more effective separation of photogenerated carriers in CdS/UiO-66-NH_2 heterostructure.

To gain deep insights of the charge carrier transfer processes in the obtained catalysts, femtosecond transient absorption spectroscopy (fs-TAS) is conducted on UiO-66-NH_2, 0.2Cd, 1.8Cd, and 2.3Cd (Fig. 4d-e and Fig. S29). The peak positions and peak intensities appear to be relatively similar, with the only difference being a reduction of peak

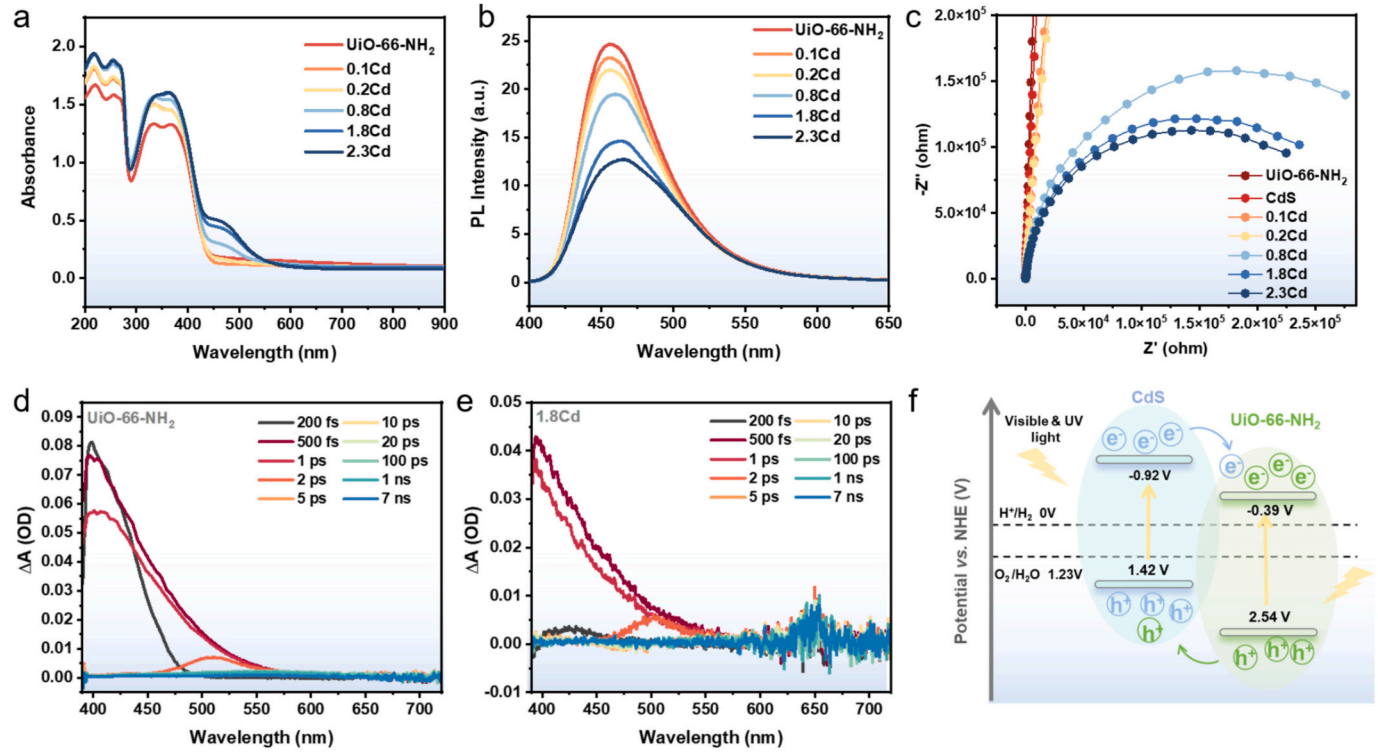

Fig. 4. (a) UV–Vis absorbance spectra, (b) PL spectra, and (c) EIS Nyquist plots for the series of samples. Time evolution of TAS for (d) UiO-66-NH_2, (e) 1.8Cd. (f) Schematic diagram of band structure of 1.8Cd.

intensity at 200 fs for 1.8Cd and 2.3Cd compared to UiO-66-NH_2. The dark grey line corresponds to a 200 fs event, which represents the charge-separated state on MOF after ligand-to-cluster charge transfer (LCCT) due to its short relaxation time. [60] The LCCT mechanism occurs when the photoexcited electron transfers from the H_2N-BDC linker to the Zr^{4+} metal centre with the generation of a photogenerated hole on the organic linker. The 420 nm peak could be attributed to the photogenerated hole trap state of UiO-66-NH_2 after light excitation. [61] Based on the significant intensity reduction observed for 1.8Cd and 2.3Cd, an ultrafast hole transfer from UiO-66-NH_2 to CdS is inferred, which facilitates spatial charge separation and suppresses charge recombination. In addition, we conducted excited-state calculations on CdS/UiO-66-NH_2 to further verify the charge transfer behavior under the excited state (Fig. S30–31 and Table S13). The excited-state electron–hole distribution shows that the electron is mainly localized on the MOF while the hole re-sides on CdS, indicating CdS-to-MOF electron transfer upon photoexcitation.

Based on the above characterization and DFT results, the proposed charge transfer pathway is illustrated in Fig. 2f. Under light irradiation, both UiO-66-NH_2 and CdS act as the light-harvesting centers, generating electron-hole pairs upon excitation. As valence band (VB) potential of UiO-66-NH_2 is more positive than that of CdS, the photogenerated holes are transferred from the VB UiO-66-NH_2 to the VB of CdS. Meanwhile, driven by the conduction band (CB) offset, the photogenerated electrons are transferred from the CB of CdS to the CB of UiO-66-NH_2. This spatial separation of holes and electrons via the heterostructure effectively suppresses the recombination of photoinduced charge carriers.

3.4. Photocatalytic water splitting

After a detailed analysis of the structural and optical properties, the photocatalytic water splitting performance of the obtained catalysts was evaluated (Fig. 5a). Interestingly, the catalytic activity displays a non-monotonic relationship with Cd loading. The catalytic activities of 0.1Cd and 0.2Cd are comparable and slightly lower than that of the pristine UiO-66-NH_2 within experimental error. In contrast, the 0.8Cd, 1.8Cd, and 2.3Cd samples exhibit significantly enhanced catalytic performance. The 1.8Cd sample exhibits the highest activity of 26.9 μmol g_{cat}^{-1} h^{-1}, more than doubling that of parent UiO-66-NH_2. These results suggest that catalysts featuring CdS species are considerably more effective for photocatalysis than those containing single-site Cd^{2+} species.

In addition, resemblance between the trend in BET surface area and the photocatalytic activity can be noticed. The correlation is quantified by a plot of photocatalytic activity against the BET surface area (Fig. 5b). Fascinatingly, the points corresponding to single-site Cd^{2+} decorations (0.1Cd, 0.2Cd) and CdS decorations (0.8Cd 1.8Cd and 2.3Cd) can both be independently fit linearly with high R factors (0.908 and 0.999, respectively) with the fitting parameters available in Supplementary Table S14. The negative slope for 0.1Cd and 0.2Cd samples (blue line) indicates that the slight improvement in BET surface area due to Cd^{2+} dispersed in the pores worsens the photocatalytic activity. Conversely, the improvement in the BET surface area for 0.8Cd 1.8Cd, and 2.3Cd samples (red line), due to CdS species benefits photocatalysis greatly. 2.3Cd underperforms 1.8Cd in the photocatalysis can be further explained by the excessive aggregation of CdS clusters. on the surface of the MOF, as evidenced by the increased average particle size and reduced specific surface area. Additionally, the enlarged CdS clusters may also cause a pore-blocking effect, resulting in a reduced surface area and loss of accessible active sites.

In addition to its promising H_2 production performance, catalytic durability and structural stability of 1.8Cd was evaluated through cycling tests. As shown in Fig. 5c, the hydrogen evolution rate remained substantially stable, retaining 91% of its initial activity after five cycles. Post-reaction characterizations, including XRD, N_2 BET, and XPS, revealed no discernible changes in the crystallinity, porosity, or chemical states of the sample (Fig. S32), indicating its great structural stability. Additionally, the Zr and Cd atomic weight content of the 1.8Cd sample before and after the reaction was tested by ICP-OES (Table S17). The minimal variation in Cd content before and after the reaction demonstrates negligible leaching of the CdS species, which further confirms the robust anchoring of the CdS on UiO-66-NH_2 MOF.

4. Conclusions and perspectives

A one-pot synthesis method of CdS-decorated UiO-66-NH_2 was devised. The incorporation of Cd can be controlled by the amount of S source (TAA) added, which forms single-site Cd^{2+} and CdS clusters in the pores, as well as CdS particles on the surface of UiO-66-NH_2. The presence of CdS clusters in the pore induces a gate-opening effect in UiO-66-NH_2 through the formation of Cd—N bonds accompanied by charge transfer from the MOF to CdS, resulting in the rotation of organic linkers and an increase in the dihedral angle. This gate-opening phenomenon significantly enhances the specific surface area and retains the pore active site accessibility of MOF after composition. Furthermore, the CdS decorations effectively suppress the recombination of photogenerated charge carriers and enhance light-harvesting capabilities in the visible light region. These synergistic effects collectively contribute to improved photocatalytic water splitting performance. This study offers valuable insights into the development of innovative synthetic strategies for constructing MOFs with co-catalysts, facilitating the advancement of more efficient photocatalytic systems.

CRediT authorship contribution statement

Qi Li: Writing – review & editing, Writing – original draft, Visualization, Investigation, Formal analysis. **Bryan Kit Yue Ng:** Writing – original draft, Formal analysis, Data curation. **Zhao-Xue Luan:** Writing

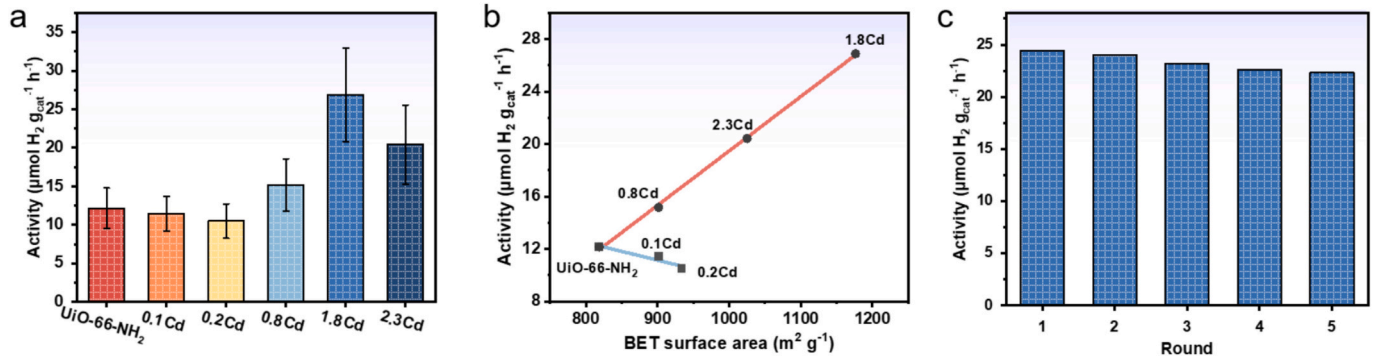

Fig. 5. (a) Photocatalytic water splitting activities performed at 120 °C with 10% *v*/v TEOA. (b) Plot of catalytic activity against BET surface area. (c) The stability test of the 1.8Cd catalyst over five cycles.

– review & editing, Writing – original draft, Visualization, Formal analysis, Data curation. **Ping-Luen Baron Ho:** Methodology, Investigation, Formal analysis, Data curation. **Daniel Woodside:** Formal analysis, Data curation. **Xiyu Zhang:** Formal analysis, Data curation. **Christopher Foo:** Formal analysis, Data curation. **Pu Zhao:** Formal analysis, Data curation. **Tai-Sing Wu:** Resources, Methodology, Investigation, Data curation. **Yun-Liang Soo:** Resources, Methodology, Data curation. **Mingjie Li:** Resources, Methodology, Data curation. **Xin-Ping Wu:** Writing – review & editing, Writing – original draft, Visualization, Resources, Funding acquisition, Formal analysis, Data curation. **Guangchao Li:** Writing – review & editing, Writing – original draft, Supervision, Resources, Project administration, Funding acquisition, Formal analysis. **Shik Chi Edman Tsang:** Writing – original draft, Supervision, Resources, Project administration, Funding acquisition.

Declaration of competing interest

The authors declare that they have no known competing financial interests or personal relationships that could have appeared to influence the work reported in this paper.

Acknowledgements

S. C. E. T. deceased on May 20, 2025.

The project was funded by the EPSRC, UK (EP/W012316/1), the Hong Kong Polytechnic University (PolyU P0049034, P0055259, P0052825), the Department of Science and Technology of Guangdong Province (GDSTC 2025A1515011688), and the National Natural Science Foundation of China (Grants W2541007, 22473042, 52394271, 52394273). The authors appreciate the BL14W1 beamline of Shanghai Synchrotron Radiation Facility (SSRF), Shanghai, China. The help from Prof. Federico Rosei (review and comments) was acknowledged.

Appendix A. Supplementary data

Supplementary data to this article can be found online at https://doi.org/10.1016/j.cej.2026.176362.

Data availability

Data will be made available on request.

References

[1] Hang Liu, Caiyun Xu, Dandan Li, H.-L. Jiang, Photocatalytic hydrogen production coupled with selective Benzylamine oxidation over MOF composites, Angew. Chem. 130 (2018) 5477–5481.
[2] Q. Wang, Q. Gao, A.M. Al-Enizi, A. Nafady, S. Ma, Recent advances in MOF-based photocatalysis: environmental remediation under visible light, Inorg. Chem. Front. 7 (2020) 300–339.
[3] K. Sun, Y. Qian, H. Jiang, Metal-organic frameworks for photocatalytic water splitting and CO_2 reduction, Angew. Chem. Int. Ed. 62 (2023) e202217565.
[4] M. Chen, Q. Zhang, L. Jiang, H. Hu, C. Wang, Z. Li, Mechanochemically incorporating magnesium sulfate into antigorite to provide active nucleation sites for efficient precipitation of cadmium ions from weak acidic solution, J. Hazard. Mater. 424 (2022) 127272.
[5] M. Yang, Y. Zhou, D. Zhang, F. Zhou, H. Ning, M. He, R. Chi, W. Yin, Highly effective and selective recovery of Gd(III) from wastewater by defective MOFs-based ion-imprinted polymer: performance and mechanism, Chem. Eng. J. 474 (2023) 145782.
[6] L. Yao, S. Zhang, R. Wang, L. Zhang, Y. Wang, W. Yin, Phosphoric acid functionalized superhydrophilic and underwater superoleophobic UiO-66/polyester fabric composite membrane for efficient oil/water separation and Gd(III) recovery, Desalination 544 (2022) 116141.
[7] Y. Gao, L. Yao, S. Zhang, Q. Yue, W. Yin, Versatile crosslinking synthesis of an EDTA-modified UiO-66-NH_2/cotton fabric composite for simultaneous capture of heavy metals and dyes and efficient degradation of organophosphate, Environ. Pollut. 316 (2023) 120622.
[8] T.K. Vo, J. Kim, J. Park, D.Q. Dao, H.B. Truong, Aminobenzoate-defected UiO-66 (Zr)-NH_2 frameworks: scalable synthesis and characterizations for adsorptive denitrogenation from model fuel, Chem. Eng. J. 481 (2024) 148570.
[9] Q. Xue, K.H. Chan, C.K. Yim, B.K.Y. Ng, T. Chen, S.J. Day, C. Tang, S. Kawaguchi, K.-Y. Wong, T.W.B. Lo, Guest-anion-induced rotation-restricted emission in UiO-66-NH_2 and advanced structure elucidation, Chem. Mater. 33 (2021) 5422–5429.
[10] T. Minh Nguyet Bui, T. Ky Vo, N. Hoang Yen Phuong, V. Hung Nguyen, V. Cuong Nguyen, Q. Hung Nguyen, N. Thi Thanh Dang, Fe(III)-incorporated UiO-66(Zr)-NH2 frameworks: microwave-assisted scalable production and their enhanced photo-fenton degradation catalytic activities, Sep. Purif. Technol. 355 (2025) 129723.
[11] T.K. Vo, M.T. Nguyen, V.C. Nguyen, J. Kim, Microwave-assisted synthesis of $MgFe_2O_4$-decorated UiO-66(Zr)-NH_2 composites for collaborative adsorption and photocatalytic degradation of tetracycline, Korean J. Chem. Eng. 39 (2022) 2532–2541.
[12] L. Shen, S. Liang, W. Wu, R. Liang, L. Wu, CdS-decorated UiO–66(NH_2) nanocomposites fabricated by a facile photodeposition process: an efficient and stable visible-light-driven photocatalyst for selective oxidation of alcohols, J. Mater. Chem. A 1 (2013) 11473.
[13] N. Sultana, P. Priyadarshini, K. Parida, UiO-66-NH_2 and its functional nanohybrids: unlocking photocatalytic potential for clean energy and environmental remediation, sustainable, Energy Fuel 9 (2025) 3458–3494.
[14] B.G. Diamond, L.I. Payne, C.H. Hendon, Ligand field tuning of d-orbital energies in metal-organic framework clusters, Commun. Chem. 6 (2023) 67.
[15] Y. Zhang, X. Hao, X. Ma, H. Liu, Z. Jin, Special Z-scheme CdS@WO_3 heterojunction modified with CoP for efficient hydrogen evolution, Int. J. Hydrog. Energy 44 (2019) 13232–13241.
[16] C. Prasad, N. Madkhali, J.S. Won, J.E. Lee, S. Sangaraju, H.Y. Choi, CdS based heterojunction for water splitting: a review, Mater. Sci. Eng., B 292 (2023) 116413.
[17] L. Cheng, Q. Xiang, Y. Liao, H. Zhang, CdS-based photocatalysts, Energy Environ. Sci. 11 (2018) 1362–1391.
[18] Q. Li, X. Li, S. Wageh, A.A. Al-Ghamdi, J. Yu, CdS/graphene nanocomposite Photocatalysts, Adv. Energy Mater. 5 (2015) 1500010.
[19] H. Xiong, Z. Liu, X. Chen, H. Wang, W. Qian, C. Zhang, A. Zheng, F. Wei, In situ imaging of the sorption-induced subcell topological flexibility of a rigid zeolite framework, Science 376 (2022) 491–496.
[20] F. Zheng, R. Chen, Y. Liu, Q. Yang, Z. Zhang, Y. Yang, Q. Ren, Z. Bao, Strengthening Intraframework interaction within flexible MOFs demonstrates simultaneous sieving acetylene from ethylene and carbon dioxide, Adv. Sci. 10 (2023) 2207127.
[21] B. Liu, X. Chen, N. Huang, S. Liu, Y. Wang, X. Lan, F. Wei, T. Wang, Imaging the dynamic influence of functional groups on metal-organic frameworks, Nat. Commun. 14 (2023) 4835.
[22] T. Luo, H.S. Jeppesen, A. Schoekel, N. Bönisch, F. Xu, R. Zhuang, Q. Huang, I. Senkovska, V. Bon, T. Heine, A. Kuc, S. Kaskel, Photocatalytic dehalogenation of aryl halides mediated by the flexible metal–organic framework MIL-53(Cr), Angew. Chem. Int. Ed. 64 (2025) e202422776.
[23] D. Fairen-Jimenez, S.A. Moggach, M.T. Wharmby, P.A. Wright, S. Parsons, T. Düren, Opening the gate: framework flexibility in ZIF-8 explored by experiments and simulations, J. Am. Chem. Soc. 133 (2011) 8900–8902.
[24] A. Modrow, D. Zargarani, R. Herges, N. Stock, The first porous MOF with photoswitchable linker molecules, Dalton Trans. 40 (2011) 4217–4222.
[25] S. Wannapaiboon, A. Schneemann, I. Hante, M. Tu, K. Epp, A.L. Semrau, C. Sternemann, M. Paulus, S.J. Baxter, G. Kieslich, R.A. Fischer, Control of structural flexibility of layered-pillared metal-organic frameworks anchored at surfaces, Nat. Commun. 10 (2019) 346.
[26] Z. Zhai, X. Zhang, J. Wang, H. Li, Y. Sun, X. Hao, Y. Qin, B. Niu, C. Li, Washable and flexible gas sensor based on UiO-66-NH_2 nanofibers membrane for highly detecting SO_2, Chem. Eng. J. 428 (2022).
[27] G. Li, T. Yoskamtorn, W. Chen, C. Foo, J. Zheng, C. Tang, S. Day, A. Zheng, M.M.-J. Li, S.C.E. Tsang, Thermal alteration in adsorption sites over SAPO-34 zeolite, Angew. Chem. Int. Ed. 61 (2022) e202204500.
[28] N. Li, J. Pang, F. Lang, X.-H. Bu, Flexible metal–organic frameworks: from local structural design to functional realization, Acc. Chem. Res. 57 (2024) 2279–2292.
[29] X. Li, E. Almatrafi, H. Wang, X. Liu, Y. Yang, C. Zhou, X. Tang, X. Ren, L. Yin, G. Zeng, D. Wang, Novel synthesis strategy for Z-scheme BiOCl/UiO-66 photocatalyst: enhanced surface area and improved Cr(VI) removal efficiency, Chem. Eng. J. 457 (2023).
[30] Y. Cao, Y. Zhao, Z. Lv, F. Song, Q. Zhong, Preparation and enhanced CO_2 adsorption capacity of UiO-66/graphene oxide composites, Ind. Eng. Chem. 27 (2015) 102–107.
[31] C. Adamo, V. Barone, Toward reliable density functional methods without adjustable parameters.: the PBE0 model, J. Chem. Phys. 110 (1999) 6158–6170.
[32] J. VandeVondele, J. Hutter, Gaussian basis sets for accurate calculations on molecular systems in gas and condensed phases, J. Chem. Phys. 127 (2007) 114105.
[33] S. Goedecker, M. Teter, J. Hutter, Separable dual-space Gaussian pseudopotentials, Phys. Rev. B 54 (1996) 1703–1710.
[34] M.E. Casida, Time-dependent density-functional theory for molecules and molecular solids, J. Mol. Struct. THEOCHEM 914 (2009) 3–18.
[35] T.D. Kühne, M. Iannuzzi, M. Del Ben, V.V. Rybkin, P. Seewald, F. Stein, T. Laino, R. Z. Khaliullin, O. Schütt, F. Schiffmann, CP2K: an electronic structure and molecular dynamics software package-quickstep: efficient and accurate electronic structure calculations, J. Chem. Phys. 152 (2020) 194103.
[36] S. Xu, C. Wang, Y. Cui, Theoretical study on influence of ligand and solvent to CdS clusters, Int. J. Quantum Chem. 111 (2011) 156–164.
[37] E.A. Butler, D.G. Peters, E.H. Swift, Hydrolysis reactions of Thioacetamide in aqueous solutions, Anal. Chem. 30 (1958) 1379–1383.
[38] D.F. Bowersox, E.H. Swift, Precipitation of cadmium sulfide from acid solutions by Thioacetamide, Anal. Chem. 30 (1958) 1288–1291.

[39] P.W. Ayers, An elementary derivation of the hard/soft-acid/base principle, J. Chem. Phys. 122 (2005) 141102.
[40] G. Wang, C.-T. He, R. Huang, J. Mao, D. Wang, Y. Li, Photoinduction of cu single atoms decorated on UiO-66-NH_2 for enhanced photocatalytic reduction of CO_2 to liquid fuels, J. Am. Chem. Soc. 142 (2020) 19339–19345.
[41] S. Brunauer, L.S. Deming, W.E. Deming, E. Teller, On a theory of the van der Waals adsorption of gases, J. Am. Chem. Soc. 62 (1940) 1723–1732.
[42] J. Mehta, S. Dhaka, A.K. Paul, S. Dayananda, A. Deep, Organophosphate hydrolase conjugated UiO-66-NH_2 MOF based highly sensitive optical detection of methyl parathion, Environ. Res. 174 (2019) 46–53.
[43] X.-Y. Xu, C. Chu, H. Fu, X.-D. Du, P. Wang, W. Zheng, C.-C. Wang, Light-responsive UiO-66-NH_2/Ag_3PO_4 MOF-nanoparticle composites for the capture and release of sulfamethoxazole, Chem. Eng. J. 350 (2018) 436–444.
[44] W. Liang, C.J. Coghlan, F. Ragon, M. Rubio-Martinez, D.M. D'Alessandro, R. Babarao, Defect engineering of UiO-66 for CO_2 and H_2O uptake - a combined experimental and simulation study, Dalton Trans. 45 (2016) 4496–4500.
[45] M.J. Katz, Z.J. Brown, Y.J. Colon, P.W. Siu, K.A. Scheidt, R.Q. Snurr, J.T. Hupp, O. K. Farha, A facile synthesis of UiO-66, UiO-67 and their derivatives, Chem. Commun. (Camb.) 49 (2013) 9449–9451.
[46] L. Wang, P. Zheng, X. Zhou, M. Xu, X. Liu, Facile fabrication of CdS/UiO-66-NH_2 heterojunction photocatalysts for efficient and stable photodegradation of pollution, J. Photochem. Photobiol., A 376 (2019) 80–87.
[47] C.A.L. Filgueiras, F. Carazza, Electronic transitions as a probe of tetrahedral versus octahedral coordination in nickel (II) complexes, J. Chem. Educ. 57 (1980) 826–827.
[48] X. Zhang, P. Huang, A. Liu, M. Zhu, A metal–organic framework for oxidative desulfurization: UIO-66(Zr) as a catalyst, Fuel 209 (2017) 417–423.
[49] A.M. Abdel-Mageed, B. Rungtaweevoranit, M. Parlinska-Wojtan, X. Pei, O. M. Yaghi, R.J. Behm, Highly active and stable single-atom cu catalysts supported by a metal-organic framework, J. Am. Chem. Soc. 141 (2019) 5201–5210.
[50] C. Xu, Y. Pan, G. Wan, H. Liu, L. Wang, H. Zhou, S.H. Yu, H.L. Jiang, Turning on visible-light photocatalytic C-H oxidation over metal-organic frameworks by introducing metal-to-cluster charge transfer, J. Am. Chem. Soc. 141 (2019) 19110–19117.
[51] R.D. Shannon, Revised effective ionic radii and systematic studies of interatomic distances in halides and chalcogenides, Acta Crystallogr., A 32 (1976) 751–767.
[52] G.A. Craig, P. Larpent, S. Kusaka, R. Matsuda, S. Kitagawa, S. Furukawa, Switchable gate-opening effect in metal-organic polyhedra assemblies through solution processing, Chem. Sci. 9 (2018) 6463–6469.
[53] X. Sun, Y. Ma, J. Zhao, D.S. Li, G. Li, L. Zhang, Y. Liu, Tuning the gate opening pressure of a flexible doubly interpenetrated metal-organic framework through ligand functionalization, Dalton Trans. 47 (2018) 13158–13163.
[54] W. Wang, G.-D. Wang, B. Zhang, X.-Y. Li, L. Hou, Q.-Y. Yang, B. Liu, Discriminatory gate-opening effect in a flexible metal-organic framework for inverse CO_2/C_2H_2 separation, Small 19 (2023) 2302975.
[55] S. Xu, C. Wang, Y. Cui, Theoretical study on influence of ligand and solvent to CdS clusters, Int. J. Quantum Chem. 111 (2011) 156–164.
[56] K. Gayathri, K. Vinothkumar, Y.N. Teja, B.M. Al-Shehri, M. Selvaraj, M. Sakar, R. G. Balakrishna, Ligand-mediated band structure engineering and physiochemical properties of UiO-66 (Zr) metal-organic frameworks (MOFs) for solar-driven degradation of dye molecules, Colloids Surf. A Physicochem. Eng. Asp. 653 (2022) 129992.
[57] R.R. Solís, M. Peñas-Garzón, C. Belver, J.J. Rodriguez, J. Bedia, Highly stable UiO-66-NH_2 by the microwave-assisted synthesis for solar photocatalytic water treatment, J. Environ. Chem. Eng. 10 (2022) 107122.
[58] Y. He, L. Shi, J. Wang, J. Yan, Y. Chen, X. Wang, Y. Song, G. Han, UiO-66-NDC (1,4-naphthalenedicarboxilic acid) as a novel fluorescent probe for the selective detection of Fe^{3+}, J. Solid State Chem. 285 (2020) 121206.
[59] H. Boaz, G.K. Rollefson, The quenching of fluorescence. Deviations from the stern-Volmer law, J. Am. Chem. Soc. 72 (1950) 3435–3443.
[60] M. Gutierrez, B. Cohen, F. Sánchez, A. Douhal, Photochemistry of Zr-based MOFs: ligand-to-cluster charge transfer, energy transfer and excimer formation, what else is there? Phys. Chem. Chem. Phys. 18 (2016) 27761–27774.
[61] Z. Lian, Z. Li, F. Wu, Y. Zhong, Y. Liu, W. Wang, J. Zi, W. Yang, Photogenerated hole traps in metal-organic-framework photocatalysts for visible-light-driven hydrogen evolution, Commun. Chem. 5 (2022) 93.
[62] C.Y. Sun, X.L. Wang, C. Qin, J.L. Jin, Z.M. Su, P. Huang, K.Z. Shao, Solvatochromic behavior of chiral mesoporous metal-organic frameworks and their applications for sensing small molecules and separating cationic dyes, Chemistry 19 (2013) 3639–3645.
[63] L. Shen, S. Liang, W. Wu, R. Liang, L. Wu, CdS-decorated UiO–66(NH_2) nanocomposites fabricated by a facile photodeposition process: an efficient and stable visible-light-driven photocatalyst for selective oxidation of alcohols, J. Mater. Chem. A 1 (2013) 11473–11482.